Using MicroCT Imaging Technique to Quantify Heat Generation Distribution Induced by Magnetic Nanoparticles for Cancer Treatments

Anilchandra Attaluri

Ronghui Ma

Liang Zhu[1]
Associate Professor
e-mail: zliang@umbc.edu

Department of Mechanical Engineering,
University of Maryland,
Baltimore County, 1000 Hilltop Circle,
Baltimore, MD 21250

Magnetic nanoparticles have been used in clinical and animal studies to generate localized heating for tumor treatments when the particles are subject to an external alternating magnetic field. Currently, since most tissue is opaque, the detailed information of the nanoparticle spreading in the tissue after injections cannot be visualized directly and is often quantified by indirect methods, such as temperature measurements, to inversely determine the particle distribution. In this study, we use a high resolution microcomputed tomography (microCT) imaging system to investigate nanoparticle concentration distribution in a tissue-equivalent agarose gel. The local density variations induced by the nanoparticles in the vicinity of the injection site can be detected and analyzed by the microCT system. Heating experiments are performed to measure the initial temperature rise rate to determine the nanoparticle-induced volumetric heat generation rates (or specific absorption rate (SAR W/m^3)) at various gel locations. A linear relationship between the measured SARs and their corresponding microCT pixel index numbers is established. The results suggest that the microCT pixel index number can be used to represent the nanoparticle concentration in the media since the SAR is proportional to the local nanoparticle concentration. Experiments are also performed to study how the injection amount, gel concentration, and nanoparticle concentration in the nanofluid affect the nanoparticle spreading in the gel. The nanoparticle transport pattern in gels suggests that convection and diffusion are important mechanisms in particle transport in the gel. Although the particle spreading patterns in the gel may not be directly applied to real tissue, we believe that the current study lays the foundation to use microCT imaging systems to quantitatively study nanoparticle distribution in opaque tumor.
[DOI: 10.1115/1.4002225]

Keywords: magnetic nanoparticles, hyperthermia, cancer, heating, temperature, microCT imaging

1 Introduction

Magnetic nanoparticles or microparticles have been proposed to heat tumor tissue in cancer treatment since the 1950s. In this method, superparamagnetic nanoparticles can deliver adequate heating to irregular and/or deep-seated tumors when exposed to a relatively low magnetic field and frequency. The heat generated by these particles when exposed to an external alternating magnetic field is mainly due to the Néel relaxation mechanism and/or the Brownian motion of particles [1,2]. Previous studies showed that iron oxides magnetite Fe_3O_4 and maghemite γ-Fe_2O_3 nanoparticles are biocompatible in the human tissue [3]. In the past decade, there have been renewed interests in using magnetic nanoparticles in cancer treatments [4–7]. Due to technical advancement in manufacturing nanosized magnetic particles, nanoparticle hyperthermia has emerged as an attractive alternative to costly and risky surgical procedures because of its few associated complications and targeted delivery of thermal energy to the tumor.

Different methods exist to deliver nanoparticles to tumor: either systemically if the blood vessels of the diseased organ are well known or by directly injecting the nanoparticles in the extracellular space of the tumor. The systemic delivery of the nanoparticles relies on the coating on the particles and its strong affinity to receptors on the tumor cells. Recently, a numerical study [8] proposed a method combining both heat and mass transfer for targeted drug delivery. In the past years, our group [9–11] investigated the feasibility of elevating the temperature of the entire tumor above a certain threshold using direct injection of nanofluid at multiple injection sites while preserving the surrounding healthy tissue from thermal damage. The direct injection method is the focus of this study and its advantage is that multiple-site injections can be exploited to cover the entire target region in the case of an irregularly shaped tumor. The success of this approach depends strongly on the nanoparticle distribution after injection, which is affected by the injection strategies including injection rate and injection amount of the nanofluid.

Previous investigations have demonstrated that particle size, particle coating, and magnetic field strength and frequency determine its heating capacity defined as the specific loss power (SLP) [1,2,12–14]. However, once the nanoparticles are manufactured, it is the spatial distribution of the particles dispersed in tissue that dominates the spatial temperature elevations. Previous experimental data have suggested that the particle concentration is not uniform after the injection and is quite different from the ferrofluid concentration [12,15–17]. Since tissue is opaque, nanoparticle distribution is usually indirectly quantified via temperature distribu-

[1]Corresponding author.

Manuscript received April 6, 2010; final manuscript received April 21, 2010; published online September 27, 2010. Assoc. Editor: Andrey Kuznetsov.

tion measured in the tumor using inverse heat transfer analyses. There lacks a direct imaging technique to study the particle distribution.

X-ray tomography nowadays is a well-established standard diagnostic tool in medical fields for inspection and testing. X-ray microcomputed tomography (microCT) offers a nondestructive way to obtain the complete high resolution three-dimensional spatial morphology of a small specimen (~cm). Recently, iron based nanoparticles have gained prominence in medical imaging [18,19]. The present work is intended to show the feasibility of using microCT technology to quantify the nanoparticle distribution in a tissue-equivalent agarose gel after direct injection. Although heat transfer in biological media can be complicated compare with agarose gel, agarose gel has similar convection/diffusion properties as that of tumor [21]. The gel has been used in the past to measure specific absorption rate (SAR) in hyperthermia studies. We hypothesize that a high resolution microCT system is sufficiently sensitive to image the density variations induced by the injected nanoparticles in the gel. Although the microCT does not allow direct visualization of individual nanoparticles, the accumulation of nanoparticles in the gel would result in a region with a much higher density than the rest of the gel area and the density distribution can be detected by the microCT system. Several previous studies [6,7] have utilized computed tomography (CT) images to study ferrofluid distribution, however, those studies are limited by their spatial resolution (~mm) and temperature resolution (~1 °C). In this study, we injected a commercially available ferrofluid containing magnetic nanoparticles. The high resolution (~μm) three-dimensional images of the density distribution were quantified to establish a correlation with the measured SAR values at various gel locations. The images were later analyzed for different injection parameters including the injection amount (0.1 cc or 0.2 cc), gel concentration (0.5%, 1%, 2%, or 4%), and ferrofluid concentration (3.9% or 5.8%) by volume of particle concentration. The spreading of the ferrofluid in the gel after injection was discussed based on the microCT pixel index variations in the gel.

2 Methods

2.1 Nanoparticle Injection and Agarose Gel. Water based ferrofluids (EMG705 series, Ferrotec (USA), Corporation, Nashua, NH) with a concentration of 3.9% or 5.8% by volume and a particle size of 10 nm were injected in an agarose gel at different infusion flow rates. The agarose gel was prepared by dispersing agarose powder (Sigma-Aldrich, Saint Louis, MO) in a 10% buffer solution (Tris-borate EDTA, Gibco BRL, Rockville, MD). The mixture was then heated until the agarose was completely dissolved. After being cooled at room temperature to 60 °C, the solution was loaded into a transparent container and was cooled further to room temperature (25 °C) until solidification. The nanofluid distribution was studied in four agarose concentrations (0.5%, 1%, 2%, and 4%). Previous experimental studies showed that higher concentration agarose gels have a microstructure similar to hard tissue [20] while lower concentration gels have a porosity similar to soft tissue such as brain.

The ferrofluid was loaded on a syringe pump (Genie Plus, Kent Scientific, Inc. Torrington, CT) that enables a precise control of the flow rate and the amount of injection. The injection amount was selected as 0.1 cc or 0.2 cc [8,9] and the injection rate was adjusted so that the region containing the nanoparticle and the ferrofluid, which appears dark in the agarose gel, is approximately having a spherical shape. Figure 1 illustrates a semitransparent agarose gel with the injected ferrofluid represented by the dark color. Our previous experiments have suggested using a very low injection rate to provide gentle pressure to the gel [8]. Flow rates of 1 μl/min, 1.25 μl/min, 2.5 μl/min, and 3 μl/min were tested to give spherical shapes in the 4%, 2%, 1%, and 0.5% gel concentrations, respectively. The injection amount of 0.1 cc or 0.2 cc were selected instead of 0.3 cc used in the previous study [8] due to the consideration of the maximum specimen size allowed in the scan chamber of the imaging system.

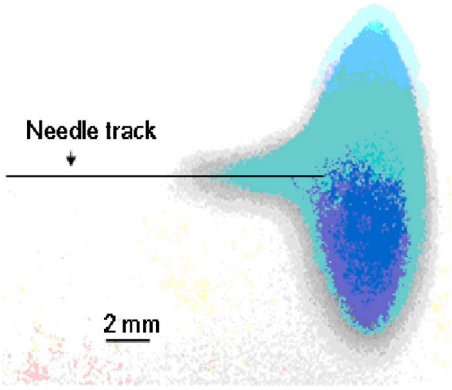

Fig. 1 Ferrofluid infused in a semitransparent agarose gel. There is limited back flow of the ferrofluid along the needle track.

2.2 MicroCT Imaging. Our previous experience on nanoparticle spreading has suggested that there is very little change in the nanoparticle spreading after injection within 24 h of the injection. In this study, we used a high resolution microCT imaging system (Skyscan 1172, Microphotonics, PA) to image the density of the agarose gel with nanoparticles. The gel block was mounted on the platform of the imaging system with the help of a stage holder. The gel block was placed in a low-density styrofoam, which would absorb little X-ray during the scan. A medium resolution scan of 17 μm (pixel size) was done at 100 kV, 100 μA without a filter. The total CT scan time was approximately less than 20 min. The images acquired from the microCT scan were reconstructed using the NRECON® software package provided by Microphotonics. Scan parameters and reconstruction parameters were kept the same for all the gel blocks in this study, therefore, the final pixel index number in the images is correlated with the same density of the sample. Each slice of the reconstructed images has a thickness of 17 μm. Maximum intensity projection images or pseudo 3D projections were generated from the reconstructed images. The density distribution was analyzed using the analysis software CTAN® (Microphotonics, PA). The change in the pixel density was analyzed in both the axial direction parallel to the needle and the radial direction.

2.3 Specific Absorption Rate Measurements. Nanoparticle heating was carried out via placing the gel block in a two-turn water cooled coil (20 cm in diameter and 7 cm in height), which is connected to a radio-frequency generator (Hotshot 2, Ameritherm, Inc., Rochester, NY). An alternative current of up to 384 A at a frequency of 183 kHz was generated through the coil and an alternating magnetic field was induced. Prior to each heating experiment, the gel compartment was kept at room temperature, so that a uniform temperature distribution can be established throughout the gel. The interference between the magnetic field and the thermocouple was found to be negligible. In the absence of any heat conduction in the gel, the volumetric heat generation rate or the SAR can be evaluated by the initial value of the transient term in the heat conduction equation [9,22–24]

$$\mathrm{SAR} = \rho c_p \left.\frac{\partial T}{\partial t}\right|_{t=0} \tag{1}$$

where T is the temperature measurements at each gel location before and after the heating was turned on and ρ and c_p are the density and the specific heat of the gel, respectively [9]. The initial slope of each curve was obtained by a linear fitting of the first four measurements of the heating curve. A minimum value of 96% for

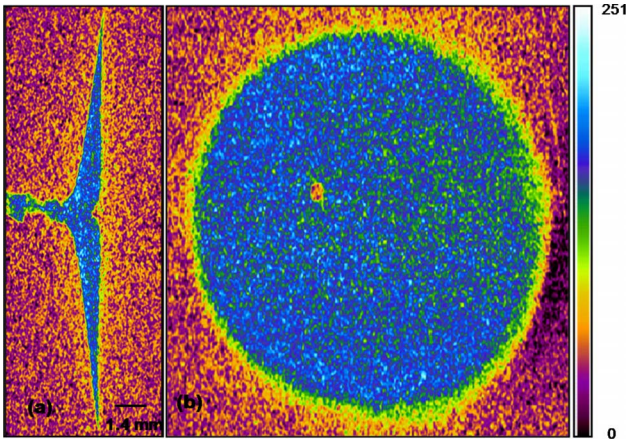

Fig. 2 Side view (*a*) and top view (*b*) of the intensity index distribution of the disk pattern from the center slice

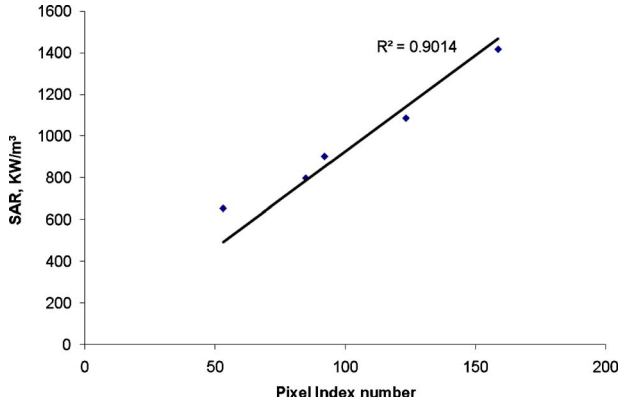

Fig. 3 Linear correlations between the SAR measurements and the pixel index numbers. Lines represent curve fitted curve and symbols denote experimental measurements.

the R^2 value was obtained for the curve fittings.

Guided by the X-ray images of the gel with ferrofluid, several fine thermocouples were inserted into the gel at locations having various pixel intensities, which represent different nanoparticle concentrations. The gel was then placed in the coil to measure the initial temperature rises at various locations and later to determine the slope of the initial temperature rising curves. All temperatures were measured and recorded by a PC based LABVIEW® program.

3 Results

A nanofluid spreading pattern was observed from the scanned images. Figure 2 provides typical pseudo three-dimensional microCT images of the density variations in the vicinity of the injection site where a disk shaped region containing the nanofluid can be seen. The top view (Fig. 2(*b*)) gives a nearly perfect circular region. The side view (Fig. 2(*a*)) illustrates the feature of the disk as well as the needle track. Back flow along the needle path is evident in the figure. The pixel index numbers shown in the microCT images seem relatively uniform in the disk region. Figure 2 also shows that infiltration of nanoparticles occurs around the edge of the high density disk.

Measuring the SAR values at various gel locations can provide a quantitative comparison to the pixel index number in the microCT images. In this experimental study, we use the microCT imaging system to identify a gel location representing a specific density (denoted by the pixel index number). Therefore, the pixel index number can be considered proportional to the nanoparticle concentration. The microCT images are used to guide the insertion of a thermocouple to that location to measure its SAR value based on Eq. (1). The relationship between the SAR magnitude and the pixel index number is illustrated in Fig. 3 where symbols represent experimental data of the SAR. A linear line is used to fit the scattered data and the fitting R^2 value is larger than 0.9. This confirms our original hypothesis that the pixel index number can be used to represent the concentration distribution of the nanoparticles since the ferrofluids used in the experiments contain the same nanoparticle concentration (3.9%). In principle, the SAR magnitude is proportional to the nanoparticle concentration in the tissue.

In this study, we also evaluated how the injection amount of the ferrofluid affects the particle spreading in the gel. As shown in Fig. 4, the lines represent the distribution of the pixel index number in the vicinity of the injection site for the nanoparticle dispersion pattern shown in Fig. 2. If we assume that the pixel index number is truly proportional to the nanoparticle concentration, the nanoparticles are dispersed in the gel quite uniformly. A few nanoparticles are seen outside the disk region. When the amount of the ferrofluid is doubled from 0.1 cc to 0.2 cc, the average pixel index number in the disk decreases by 20% while the radius of the disk region increases by almost 40%.

The relationship between the nanoparticle dispersion and the gel concentration is illustrated in Fig. 5. Smaller gel concentrations should result in higher porosity and less flow resistance to the ferrofluid and the nanoparticles. As shown in the measured disk span in the figure, nanoparticles are spreading farther away

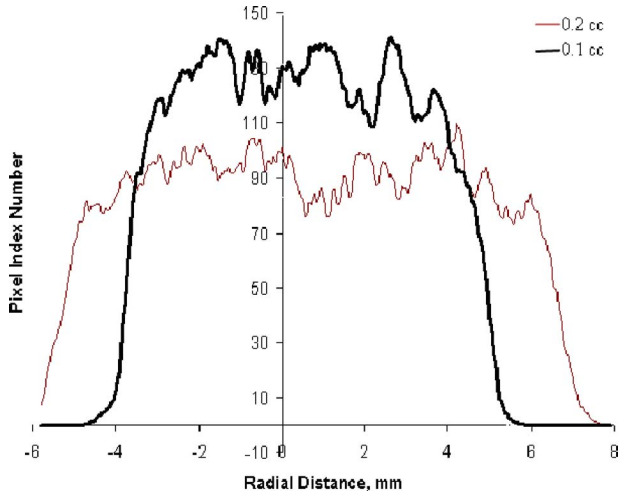

Fig. 4 Pixel density profile along the radial distance for the particle spreading pattern in Fig. 3

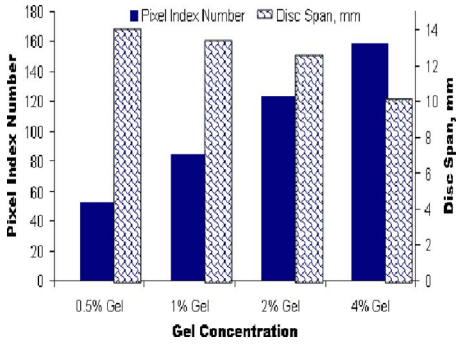

Fig. 5 Variations of the average pixel index number inside the disk and the disk diameter as a function of the gel concentration. The left *y*-axis represents the pixel index and the right *y*-axis represents the disk diameter.

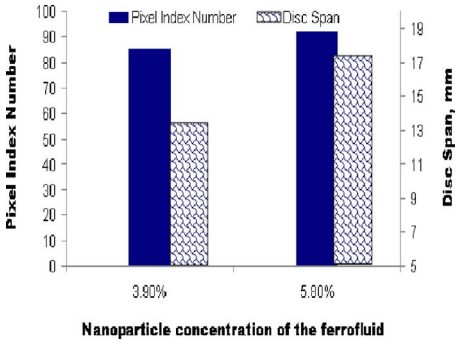

Fig. 6 Variations of the pixel index number and the disk span affected by the magnetic particle concentration in the injected ferrofluid

from the injection site when the gel concentration is low. The diameter of the disk increases from 10 mm to 12.8 mm when the gel concentration decreases by half (from 4% to 2%). More than 36% and 42% increase in the disk diameter (13.6 mm and 14.2 mm versus 10 mm) is observed when the gel concentration further decreases to 1% and 0.5%, respectively. It is clear that from the solid bars representing the pixel index number shown in Fig. 5, the dependence of the pixel index number on the gel concentration is reversed. The nanoparticle concentration inside the disk decreases by 25% when the gel concentration is lowered from 4% to 2%. Similarly, when the gel concentration is lowered from 4% to 0.5%, the decrease in the concentration of the nanoparticles is more than 63%.

Figure 6 illustrates the effect of nanoparticle concentration of the ferrofluid. Two nanoparticle concentrations of the ferrofluid (3.9% and 5.8%) are commercially available from the company. Using the same injection amount and injection rate, the ferrofluid with a higher magnetic particle concentration (5.8%) should contain more nanoparticles in the injected solution. It is not a surprise to see that both the pixel index number and the disk diameter are bigger in the images using the 5.8% ferrofluid than that using the 3.9% ferrofluid. The pixel index number only changes slightly from one ferrofluid concentration to another (84 versus 92), implying more concentrated nanoparticles surrounding the injection site when higher ferrofluid concentration is used. Due to increased number of nanoparticles in the injected amount with the 5.8%, the disk span also increases from 13.3 mm using the 3.9% ferrofluid to 17.7 mm with the 5.8% ferrofluid.

4 Discussion and Conclusions

Nanoparticle transport in tissue is a complicated process that involves nanofluid flow in the extracellular matrix of tissues, convection and diffusion of the particles in the fluid phase, deposition of the nanoparticles on the solid structure, and particle agglomeration. The complex heterogeneous structure of tissues and the deformation and breakage of a tissue induced by injection add additional difficulty in understanding the nanoparticle transport behavior during an injection. Due to the opaque nature of tissue and the insufficient techniques for characterization of nanoparticle concentration distribution, the understanding of nanoparticle transport in tissue remains limited.

Tissue equivalent phantom gels have been used in the past to study drug delivery in a tissue, considering that a gel is composed of a solid matrix with pores. The gel concentration and solidification temperature can be adjusted to mimic transport properties of various tissues, including tumors. One limitation of using gel to study nanoparticle transport in tumor is the homogeneous structure in comparison to the complicated tumor morphology heterogeneity and the different thresholds for the occurrence of pressure-induced breakage. Another limitation is the absence of vasculature in gels. However, gels are semitransparent porous materials and can provide visualization of drug spreading in drug delivery study. In the current investigation, using gel provides an easy way to identify the locations of the temperature sensors used in the SAR measurements. In principle, the local average SAR distribution depends on the number of nanoparticles per unit volume. Therefore, the comparison between the heating experiments and the microCT quantification can be used to establish a correlation between the SAR magnitude and the local nanoparticle concentration. Although CT has been used to visualize ferrofluid in the tissue in previous studies [6,7], the CT images were only a qualitative method to verify the total volume of the ferrofluid after injections. To the best of our knowledge, the current study is the first to establish quantitative relationship between the SAR and the microCT pixel index number, which is proportional to the local nanoparticle density.

The distinctive disk shape of ferrofluid spreading observed in the obtained 3D images suggested that they may be due to the delicate nature of the gel. Unlike real tissue, which can sustain sufficiently high pressure elevation without breakage, gels typically have a very low tolerance to pressure rise. It is highly possible that the disk shape obtained in experiments is a direct result of a tearing created by the injection needle. Once a crack is formed, the ferrofluid driven by the injection pressure tends to move along the vertical plane to further create a disk shaped cavity with its main axis along the vertical direction, as shown in Fig. 2. This explains the observation of a nearly uniform nanoparticle concentration within the disk. We also consider that the nanoparticles do not simply fill up the crack, rather, particle convection and diffusion have appreciable contribution to the spreading of ferrofluid in gels. Driven by the elevated infusion pressure, convection, diffusion, and deposition of the nanoparticles also occur in the porous gel structure adjacent to the cavity. Our observation and analysis were consistent with a previous work done by Nicholson [25] and Nicholson and Sykova [26] in the tissue environment. It suggested that the ferrofluid forms a cavity in the tissue that expands with further injected amounts and infiltrates in the extracellular space. Our results agree with the above prediction except for the time taken for the diffusion to occur, which may be attributed to the presence of blood perfusion in the tissue environment in their study.

The combined mechanism of nanoparticle transport by formation of a cavity at the injection site and particle convection and diffusion on the boundary can explain the ferrofluid spreading patterns observed in the experiment. For example, when doubling the injection volume of the ferrofluid, the increased injection amount causes formation of a larger cavity near the injection site and extended injection duration. The larger boundary area and longer injection time may facilitate particle convection and diffusion, thereby, leading to a larger disk span and a reduced average particle concentration, as shown in Fig. 4. Another observation is that the particle concentration in the disk region increases with the gel concentration while the disk span exhibits opposite trend. This can be explained by the deformation properties of gels of different concentrations. Typically, gels of low concentrations are easier to break and are more prone to deformation under the infusion pressure. They also have larger pores that not only impose less resistance to ferrofluid but also make particle penetration easier. With these properties, injection in softer gels tends to create larger cavity and the effect of convection and diffusion are more pronounced. The enhanced infiltration of the particles in the gels causes a large ferrofluid spreading region and reduces the average particle concentration.

The experiment with different ferrofluid concentration suggests that the concentration can substantially affect the spreading volume. We consider this observation a strong proof of the substantial contribution of convection and diffusion to nanoparticle transport in gels. In the absence of convection and diffusion, ferrofluids of different concentration should produce the same spreading volume if other injection parameters, such as volume, injection rate,

and gel properties, remain the same. However, the significant increase in the spreading volume for ferrofluid of higher concentration demonstrates that it is convection and diffusion that cause enhanced particle spreading in the gel. This is consistent with the measurements in a previous study [12] that the heat generation rate did not increase by 100% when the particle concentration was doubled.

In conclusion, our studies have shown the feasibility of using a high resolution microCT imaging system to obtain the 3D nanoparticle concentration distribution induced by directly injected nanoparticles in the gel. Although the particle spreading patterns in the gel may not be directly applied to real tissue, we believe that the current study lays the foundation to use microCT imaging systems to quantitatively study nanoparticle distribution in opaque tumor. The quantification of the relationship between the pixel index number and the nanoparticle concentration based on heat transfer experiments in this study will further help understand the distribution of the volumetric heat generation rate induced by nanoparticles. The investigation of nanoparticle transport pattern in gels suggests that convection and diffusion are important mechanisms for nanoparticle transport in porous structures. Our long term goal is to enhance treatment planning for the required thermal dose at each injection site in nanoparticle hyperthermia.

Acknowledgment

The authors are gratefully acknowledging the financial support from the NSF research award (Grant No. CBET-0828728) and the NSF-MRI award (Grant No. CBET-0821236). The research was performed in partial fulfillmen of the requirements of the Ph.D. degrfee from University of Maryland Baltimore County by Anilchandra Attaluri.

References

[1] Hergt, R., Andra, W., d'Ambly, C. G., Hilger, I., Kaiser, W. A., Richter, U., and Schmidt, H., 1998, "Physical Limits of Hyperthermia Using Magnetite Fine Particles," IEEE Trans. Magn., **34**, pp. 3745–3754.

[2] Rosensweig, R. E., 2002, "Heating Magnetic Fluid With Alternating Magnetic Field," J. Magn. Magn. Mater., **252**, pp. 370–374.

[3] Moroz, P., Jones, S. K., and Gray, B. N., 2002, "Magnetically Mediated Hyperthermia: Current Status and Future Directions," Int. J. Hyperthermia, **18**(4), pp. 267–284.

[4] Hilger, I., Hergt, R., and Kaiser, W. A., 2005, "Towards Breast Cancer Treatment by Magnetic Heating," J. Magn. Magn. Mater., **293**, pp. 314–319.

[5] Hergt, R., Hiergeist, R., Hilger, I., Kaiser, W. A., Lapatnikov, Y., Margel, S., and Richter, U., 2004, "Maghemite nanoparticles With Very High AC-Losses for Application in RF-Magnetic Hyperthermia," J. Magn. Magn. Mater., **270**, pp. 345–357.

[6] Wust, P., Gneveckow, U., Johannsen, M., Bohmer, D., Henkel, T., Kahmann, F., Sehouli, J., Felix, R., Ricke, J., and Jordan, A., 2006, "Magnetic Nanoparticles for Interstitial Thermotherapy—Feasibility, Tolerance and Achieved Temperatures," Int. J. Hyperthermia, **22**(8), pp. 673–685.

[7] Johannsen, M., Gneveckow, U., Thiesen, B., Taymoorian, K., Cho, C. H., Waldofner, N., Scholz, R., Jordan, A., Loening, S. A., and Wust, P., 2007, "Thermotherapy of Prostate Cancer Using Magnetic Nanoparticles—Feasibility, Imaging, and Three-Dimensional Temperature Distribution," Eur. Urol., **52**(6), pp. 1653–1662.

[8] Zhang, A., Mi, X., Yang, G., and Xu, X. L., 2009, "Numerical Study of Thermally Targeted Liposomal Drug Delivery in Tumor," J. Heat Transfer, **131**(4), p. 043209.

[9] Salloum, M., Ma, R., Weeks, D., and Zhu, L., 2008, "Controlling Nanoparticle Delivery in Hyperthermia for Cancer Treatment: Experimental Study in Agarose Gel," Int. J. Hyperthermia, **24**, pp. 337–345.

[10] Salloum, M., Ma, R., and Zhu, L., 2008, "An In-Vivo Experimental Study of Temperature Elevations in Animal Tissue During Magnetic Nanoparticle Hyperthermia," Int. J. Hyperthermia, **24**, pp. 589–601.

[11] Salloum, M., Ma, R., and Zhu, L., 2009, "Enhancement in Treatment Planning For Magnetic Nanoparticle Hyperthermia: Optimization of the Heat Absorption Pattern," Int. J. Hyperthermia, **25**, pp. 309–321.

[12] Masuko, Y., Tazawa, K., Viroonchatapan, E., Takemori, S., Shimizu, T., Fujimaki, M., Nagae, H., Sato, H., and Horikoshi, I., 1995, "Possibility of Thermosensitive Magnetoliposomes as a New Agent for Electromagnetic Induced Hyperthermia," Biol. Pharm. Bull., **18**, pp. 1802–1804.

[13] Lv, Y.-G., Deng, Z.-S., and Liu, J., 2005, "3-D Numerical Study on the Induced Heating Effects of Embedded Micro/Nanoparticles on Human Body Subject to External Medical Electromagnetic Field," IEEE Trans. Nanobiosci., **4**, pp. 284–294.

[14] Hergt, R., Hiergeist, R., Zeisberger, M., Glockl, G., Weitschies, W., Ramirez, L. P., Hilger, I., and Kaiser, W. A., 2004, "Enhancement of AC-Losses of Magnetic Nanoparticles for Heating Applications," J. Magn. Magn. Mater., **280**, pp. 358–368.

[15] Johannsen, M., Jordan, A., Scholz, R., Koch, M., Lein, M., Deger, S., Roigas, J., Jung, K., and Loening, S. A., 2004, "Evaluation of Magnetic Fluid Hyperthermia in a Standard Rat Model of Prostate Cancer," J. Endourol, **18**(5), pp. 495–500.

[16] Johannsen, M., Thiesen, B., Jordan, A., Taymoorian, K., Gneveckow, U., Waldofner, N., Scholz, R., Koch, M., Lein, M., Jung, K., and Loening, S. A., 2005, "Magnetic Fluid Hyperthermia (MFH) Reduces Prostate Cancer Growth in the Orthotopic Dunning R3327 Rat Model," Prostate, **64**(3), pp. 283–292.

[17] Bruners, P., Braunschweig, T., Hodenius, M., Pietsch, H., Penzkofer, T., Baumann, M., Günther, R. W., Schmitz-Rode, T., and Mahnken, A. H., 2010, "Thermoablation of Malignant Kidney Tumors Using Magnetic Nanoparticles: An In-Vivo Feasibility Study in a Rabbit Model," Cardiovasc. Intervent Radiol., **33**(1), pp. 127–134.

[18] Corot, C., Robert, P., Idée, J. M., and Port, M., 2006, "Recent Advances in Iron Oxide Nanocrystal Technology for Medical Imaging," Adv. Drug Delivery Rev., **58**, pp. 1471–1504.

[19] Yu, Y., and Sun, D., 2010, "Superparamagnetic Iron Oxide Nanoparticle 'Theranostics' for Multimodality Tumor Imaging, Gene Delivery, Targeted Drug and Prodrug Delivery," Expert Review of Clinical Pharmacology, **3**(1), pp. 117–130.

[20] Jain, R. K., 1999, "Transport of Molecules, Particles, and Cells in Solid Tumors," Annu. Rev. Biomed. Eng., **1**, pp. 241–263.

[21] Mahjoob, S., and Vafai, K., 2010, "Analysis of Bioheat Transport Through a Dual Layer Biological Media," J. Heat Transfer, **132**(3), p. 031101.

[22] Chen, Z. J., Broaddus, W. C., Viswanathan, R. R., Raghavan, R., and Gillies, G. T., 2002, "Intraparenchymal Drug Delivery via Positive-Pressure Infusion: Experimental and Modeling Studies of Poroelasticity in Brain Phantom Gels," IEEE Trans. Biomed. Eng., **49**, pp. 85–96.

[23] Zhu, L., Xu, L. X., and Chencinski, N., 1998, "Quantification of the 3-D Electromagnetic Power Absorption Rate in Tissue During Transurethral Prostatic Microwave Thermotherapy Using Heat Transfer Model," IEEE Trans. Biomed. Eng., **45**, pp. 1163–1172.

[24] Wang, X., Gu, H., and Yang, Z., 2005, "The Heating Effect of Magnetic Fluids in an Alternating Magnetic Field," J. Magn. Magn. Mater., **293**, pp. 334–340.

[25] Nicholson, C., 1985, "Diffusion From an Injected Volume of a Substance in Brain Tissue With Arbitrary Volume Fraction and Tortuosity," Brain Res., **333**, pp. 325–329.

[26] Nicholson, C., and Sykova, E., 1998, "Extracellular Space Revealed by Diffusion Analysis," Trends Neurosci., **21**, pp. 207–215.